Electrical conductivity of metasomatized lithology in subcontinental lithosphere

Ye Peng, Geeth Manthilake, Mainak Mookherjee

Revision 1

Electrical conductivity of metasomatized lithology in subcontinental lithosphere

Ye Peng[1*], Geeth Manthilake[2], and Mainak Mookherjee[1]

[1]Earth Materials Laboratory, Department of Earth, Ocean and Atmospheric Sciences, Florida State University, Tallahassee, FL, 32306 USA.

[2]Laboratoire Magmas et Volcans, CNRS, IRD, OPGC, Université Clermont Auvergne, Clermont-Ferrand, 63000 France.

[*]Corresponding author: Ye Peng (yp16b@my.fsu.edu)

Abstract

A plausible origin of the seismically observed mid-lithospheric discontinuity (MLD) in the subcontinental lithosphere is mantle metasomatism. The metasomatized mantle is likely to stabilize hydrous phases such as amphiboles. The existing electrical conductivity data on amphiboles vary significantly. The electrical conductivity data on hornblendite is much higher than the recent data on tremolite. Thus, if hornblendite truly represents the amphibole varieties in MLD regions, then it is likely that amphibole will cause high electrical conductivity anomalies at MLD depths. However, this is inconsistent with the magnetotelluric observations across MLD depths. Hence, to better understand this discrepancy in electrical conductivity data of amphiboles and to evaluate whether MLD could be caused by metasomatism, we determined the electrical conductivity of a natural metasomatized rock sample. The metasomatized rock sample consists of ~87% diopside pyroxene, ~9% sodium-bearing tremolite amphibole, and ~3% albite feldspar. We

collected the electrical conductivity data at ~3.0 GPa, i.e., the depth relevant to MLD. We also spanned a temperature range between 400 to 1000 K. We found that the electrical conductivity of this metasomatized rock sample increases with temperature. The temperature dependence of the electrical conductivity exhibits two distinct regimes- at low temperatures <700 K, the electrical conductivity is dominated by the conduction in the solid state. At temperatures >775 K, the conductivity increases, and it is likely to be dominated by the conduction of aqueous fluids due to partial dehydration. The main distinction between the current study and the prior studies on the electrical conductivity of amphiboles or amphibole-bearing rocks is the sodium (Na) content in amphiboles of the assemblage. And it is likely that the higher Na content in amphiboles leads to the higher electrical conductivity. Pargasite and edenite amphiboles are the most common amphibole varieties in the metasomatized mantle and our study on Na-bearing tremolite is the closest analog of these amphiboles. Comparison of the electrical conductivity results with the magnetotelluric observations limits the amphibole abundance at MLD depths to <1.5%. Such a low modal proportion of amphiboles could only reduce the shear seismic wave velocity by 0.4-0.5%, which is significantly lower than the observed velocity reduction of 2-6%. Thus, it might be challenging to explain both seismic and magnetotelluric observations at MLD simultaneously.

Key Points: Mid-lithospheric discontinuity (MLD), Electrical conductivity, Metasomatized rock, Diopside, Amphibole

Introduction

Recent high-frequency seismic data have revealed a seismic discontinuity in the subcontinental lithosphere at a depth range of 60-160 km. This is often referred to as the mid-lithospheric discontinuity (MLD) and is characterized by a 2-6% reduction in the shear seismic wave velocity (Rychert and Shearer, 2009; Romanowicz, 2009; Abt et al., 2010; Fischer et al., 2010). The thickness of the discontinuity typically varies between 10-20 km (Fischer et al., 2010).

Although MLDs are found across all cratons, their origin is poorly understood. A variety of mechanisms have been proposed to explain the observed shear velocity anomaly at MLD depths (Selway et al., 2015; Karato et al., 2015). The most plausible mechanisms include: the presence of partial melts (Thybo, 2006), elastically accommodated grain boundary sliding (Karato et al., 2015; Karato and Park, 2019), seismic anisotropy (Yuan and Romanowicz, 2010; Sodoudi et al., 2013; Wirth and Long, 2014; Ford et al., 2016), and mantle metasomatism or frozen-in melts (Savage and Silver, 2008; Sodoudi et al., 2013; Hansen et al., 2015; Rader et al., 2015, Selway et al., 2015; Saha et al., 2018; Peng and Mookherjee, 2020; Saha et al., 2021).

Mantle metasomatism alters the "dry" mantle lithology and often stabilizes carbonates and hydrous minerals such as amphiboles and phlogopite. The xenoliths formed at pressures associated with MLD depths indicate that at least ~25% of these are amphibole-bearing, ~90% are phlogopite-bearing, and less contains carbonates (Rader et al., 2015). While the presence of amphiboles in MLD tends to lower the shear seismic wave velocity (Selway et al., 2015; Peng and Mookherjee, 2020; Saha et al., 2021), it may also lead to anomalously high electrical conductivity based on the measurement of hornblendite (Wang et al., 2012). The study showed that when the temperature is higher than ~760-840 K, the electrical conductivity of hornblendite is enhanced due to the dehydration-oxidation reaction, which is about 10^4-10^6 higher than that of olivine (Wang et al., 2012). This, however, is contrary to magnetotelluric (MT) observations, since there is no globally

recognized anomaly in the electrical conductivity at MLD depths (Meqbel et al., 2014; Yang et al., 2015; Selway, 2019, Karato and Park, 2019). The inconsistency between the MT observations and expected electrical conductivity is one of the biggest criticisms of the mantle metasomatism mechanism (Karato and Park, 2019). However, a recent experimental study found that the electrical conductivity of tremolite amphibole is much lower than previously thought, about 10^3-10^5 lower than that of hornblendite. It only exceeds the conductivity of olivine by one order of magnitude at temperatures <1123 K, i.e., the melting temperature (Shen et al., 2020). Therefore, the role of amphiboles in the electrical conductivity of the mantle is ambiguous and it certainly requires further study.

To better understand the effect of hydrous phases on the electrical conductivity of metasomatized lithology, we conducted experiments to constrain the electrical conductivity on a natural metasomatized rock consisting dominantly of pyroxene, amphibole, and feldspar under conditions relevant for MLD, i.e., at ~3.0 GPa and ~400-1000 K. We then used the experimental results to determine the conductivity-depth profiles for the metasomatized cratonic mantle and evaluate whether mantle metasomatism, i.e., metasomatic amphiboles, will cause anomalously high electrical conductivity at MLD depths.

Methods

We characterized the mineral phases of the natural rock sample using Raman spectroscopy at ambient conditions (**Figure 1**). To identify the minerals, we used HORIBA LabRAM HR Evolution Raman spectrometer with a Nd:YAG laser (λ= 532 nm) at the Earth Materials Laboratory, Department of Earth, Ocean, and Atmospheric Sciences, Florida State University, Tallahassee. We also investigated the composition of each mineral phase using electron probe

89 microanalysis (EPMA). We used Cameca SxFive-Tactis at the Laboratoire Magmas et Volcans,
90 Clermont-Ferrand, France, with an accelerating voltage of 15 kV and a steady beam current of 20
91 nA. We also obtained the energy dispersive X-ray spectroscopy (EDS) chemical mapping of the
92 sample using the scanning electron microscope (SEM) with JEOL JSM-5910LV (**Figure S1**). We
93 determined the modal abundances using ImageJ open-source package (Schneider et al., 2012). We
94 found that the sample consists of ~87% pyroxene, ~9% amphibole, and ~3% feldspar (**Table 1**).
95 The stoichiometry of pyroxene is dominated by diopside [$(Mg_{1.02}Ca_{0.85}Na_{0.09}Al_{0.06})(Si_{1.99}Al_{0.01})$
96 O_6], while amphibole is Na-rich tremolite [$(Na_{0.19}K_{0.03})(Ca_{1.61}Na_{0.39})(Mg_{5.09}Fe_{0.02}Ti_{0.01})(Si_{7.75}$
97 $Al_{0.29})O_{22}(OH)_2$], and feldspar is dominantly albite [$Na_{1.09}K_{0.01}Al_{1.03}Si_{2.94}O_8$] (**Table 1**).

98 We performed the high pressure and temperature electrical conductivity experiment in a
99 1500-ton split-cylinder type multi-anvil apparatus installed at the Laboratoire Magmas et Volcans,
100 Clermont-Ferrand, France. We used an 18/11 assembly, i.e., an edge length of 18 mm for the
101 Cr_2O_3-doped MgO octahedral pressure medium and a truncated edge length of 11 mm for the eight
102 tungsten carbide (WC) anvils. We placed the cylindrical sample specimen in the MgO cylindrical
103 sleeve to electrically insulate the sample from the furnace during the measurements (**Figure S1**).
104 In addition, we placed two nickel (Ni) disks at two ends of the sample. These two Ni disks serve
105 as electrodes and also buffer the oxygen fugacity (f_{O2}) close to Ni-NiO buffer. We monitored the
106 temperature of the sample using a $W_{95}Re_5$-$W_{74}Re_{26}$ thermocouple junction placed at one side of
107 the sample. We placed another $W_{95}Re_5$ wire at the opposite side of the sample and used two
108 opposing $W_{95}Re_5$ wires that emerged at the top and bottom of the sample to collect the impedance
109 spectra for the electrical conductivity measurements. We used a 25 μm thick Re foil as the furnace.
110 To enhance effective heating and minimize thermal loss, i.e., to insulate, we also used a ZrO_2
111 sleeve surrounding the Re-furnace (**Figure S1**). To eliminate the influence of absorbed moisture

112 from the atmosphere and exposure to contaminations, we baked the ceramic assembly parts in a
113 high-temperature furnace at 1273 K for >12 hours. We stored all the heat-treated ceramic parts in
114 a high-vacuum furnace (<100 mTorr) at 398 K overnight.

115 For the electrical conductivity measurements, we analyzed the impedance spectroscopy
116 using the ModuLabMTS impedance/gain-phase analyzer over a frequency range of 10^6-10^1 Hz.
117 Before measuring the temperature dependence of the electrical conductivity of the sample, first,
118 we held the pressure constant at 3.0 GPa and kept the sample at 500 K for more than 6 hours.
119 While maintaining a constant temperature of 500 K, we measured the electrical resistance of the
120 sample at regular time intervals to ensure that the sample resistance reached a steady value. We
121 noted that the steady-state resistance is about 1 order of magnitude lower than the resistance
122 measured at the very beginning (**Figure 2**). This step is crucial to ensure the removal of the
123 absorbed moisture in the assembly, which could otherwise influence the electrical conductivity
124 measurements at higher temperatures (Manthilake et al., 2015). Then we collected the impedance
125 spectra over a temperature range of 300-1000 K at a step of ~50 K. Below 700 K, we heated and
126 cooled the sample and found that the electrical resistance for the heating and cooling path was
127 reproducible. This minimizes the uncertainty of the electrical conductivity measurements. After
128 this heating and cooling cycle, we collected the spectra in a continuous heating and cooling cycle
129 reaching 1000 K.

130 Following the electrical conductivity measurements, we investigated the cross-section of
131 the experimental run product using EPMA and EDS chemical mapping using SEM. We identified
132 the chemical compositions of each mineral phase after dehydration reaction (**Table 1**).

133 The impedance spectra of a polycrystalline sample can be better understood in terms of a
134 resistor-capacitor (R-C) or resistor-constant phase element (R-CPE) circuit. We obtained the

resistance of the polycrystalline sample by fitting the impedance spectra to appropriate RC/R-CPE circuits. We determined the electrical conductivity of the sample by the formulation: $\sigma=L/(RS)$, where σ is the electrical conductivity in "S/m", R is the resistance in "Ω", L is the length of the cylindrical sample in "m", and S is the cross-sectional area of the cylindrical sample in "m^2". The sample length and diameter measured before the experiment were ~1.7 mm in length and ~1.0 mm in diameter. Similar aspect ratios have been successfully used in previous electrical conductivity measurements, particularly when the samples are cored out of natural rocks rather than synthesized using hot-pressed methods from powdered samples (Manthilake et al., 2015, 2016, 2021). After we recovered the sample, we measured the sample length ~1.7 mm, i.e., it remained unchanged. This is very likely due to the facts that the sample used in our study is a natural rock rather than a powdered sample, and the experimental conditions were modest ~3 GPa which didn't affect the length of the sample. Since the sample is cut and polished along the length of the cylindrical core, we were unable to directly measure the diameter of the recovered sample. Based on the fact that the length remained unaffected, we used the length and diameter of the sample before the experiments to estimate the electrical conductivity.

To ensure that we are measuring the electrical conductivity of the sample and our results are not affected by the sample assembly, we also measured the electrical resistivity of the assembly. The electrical resistivity of the sample is much lower than that of the insulation resistance of the sample assembly (MgO), i.e., the electrical conductivity of the sample is significantly greater than that of the assembly (**Figure S2**).

Results

We analyzed the electrical conductivity of the sample using the impedance spectra which are often represented in a Cole-Cole plot with the imaginary part of the impedance plotted in the ordinate and the real part of the impedance plotted in the abscissa. At low temperatures, <700 K, all the spectra display a semicircular arc over the whole frequency range (**Figure S3**). The radius of the semicircular arc is proportional to the electrical resistivity, i.e., inversely proportional to the electrical conductivity. With increasing temperature, the radius of the semicircular arc continues to shrink, indicating that the electrical resistivity reduces or conversely the electrical conductivity increases with temperature. At temperatures >775 K, an additional arc is observed in the low-frequency range (**Figure S3**). The separation of the two arcs possibly indicates two conductive paths, one through the grain interior and the other one along the grain boundary. This is very likely due to the dehydration of the amphibole-bearing rock sample which generates two conductive phases operating in series, i.e., the original solid phase and the aqueous fluid phase interconnected along the grain boundaries.

The temperature dependence of the electrical conductivity exhibits a linear relationship before and after dehydration and both could be well described by the Arrhenius relationship:

$$\sigma = \sigma_0 \exp\left(\frac{-\Delta H}{RT}\right), \quad (1)$$

where σ_0 is a pre-exponential constant, R is the gas constant, and ΔH is the activation enthalpy. The activation enthalpies are respectively 0.188±0.003 eV and 0.48±0.03 eV before and after dehydration (**Figure 2**, **Table 2**). The increase in the activation enthalpy of the different segments is likely due to the dehydration reaction of the amphibole phase in the sample. The release of aqueous fluids often causes the change of slope i.e., activation enthalpy in the temperature-dependent electrical conductivity of hydrous phases. The activation enthalpy after dehydration for our study, i.e., the T_2 segment between 775 K and 1000 K, is very similar to the activation enthalpy

~0.5 eV in the T_3 segment of the tremolite sample, where the conduction mechanism is dominant by the flow of aqueous fluids (Shen et al., 2020) (**Figure 3**, **Table 2**).

The temperature range where the slope change occurs generally depends on the specific mineral assemblage and its thermal stability (Manthilake et al., 2015, 2016; Pommier and Evans, 2017; Pommier et al., 2019). The experimental study on pargasitic-edenitic amphiboles indicates that these amphibole phases are stable till 1373 K (Mandler and Grove, 2016). However, in our study, amphibole starts to dehydrate at ~775 K. An earlier study on the hornblende-actinolite-bearing rock (hornblendite) at 0.5 GPa exhibits two distinct stages of the temperature dependence of electrical conductivity, and the slope changes at ~736-760 K. Similarly, the plagioclase-hornblende-bearing rock (plagioclase hornblendite) also undergoes the discontinuous increase of the electrical conductivity at similar temperatures, i.e., ~797-840 K (**Figure 3**, **Table 2**) (Wang et al, 2012). It is not surprising that amphiboles show much lower dehydration temperatures in a multi-phase rock. The stability field of amphiboles decreases when competing with other phases, like diopside and albite.

We also noted that the electrical conductivity of our diopside-tremolite-albite sample is higher than that of pure clinopyroxene (Yang et al., 2011) or pure tremolite (Shen et al., 2020) by a factor of 10^3-10^4, especially when the temperature is lower than 1000 K (**Figure 3**). These electrical conductivity experiments on clinopyroxene, plagioclase, and amphibole were conducted at different pressures. The effect of pressure on the electrical conductivity is found to be negligible (Yang et al., 2011, 2012; Shen et al., 2020; Hu et al., 2018). Recent experiments on Fe-bearing amphibole indicated that the total Fe content influences the electrical conductivity of amphiboles. Upon heating, the sample loses hydrogen and in the process oxides the iron ($Fe^{2+} \rightarrow Fe^{3+}$), which in turn enhances the electrical conductivity via hopping of electrons (Hu et al., 2018). However,

the total Fe content of our sample is as low as ~0.12 wt.% and yet we found that our electrical conductivity results are very high, especially in the solid state (**Figure 3**). This high electrical conductivity cannot be attributed to Fe content. We found that the Na_2O content in our sample, 2.24 wt.%, is greater than that of all the amphibole samples examined in earlier electrical conductivity studies, i.e., 0.12 wt.% in tremolite (Shen et al., 2020); ~0.38 wt.% in Fe-bearing amphibole (Hu et al., 2018) and 1.44-1.75 wt.% in amphibole-bearing rocks (Wang et al., 2012). The alkali cation, i.e., Na, occupies the alkali (A) site in the crystal structure of amphiboles and the A site is often vacant in many amphibole end members including tremolite. It is very likely that Na is loosely bound in the large A site in amphiboles. The A sites are connected to each other to form channels along [001] direction that is likely to further facilitate the mobility of the Na^+ ions. Similar high electrical conductivity has been observed in liebermannite which also has tunnels that promote the migration of alkali cations (He et al., 2016; Manthilake et al., 2020). Also, fast ionic conduction in solid state has been observed in albite, where Na^+ ions undergo faster diffusion via the alkali ion cavities in the albite aluminosilicate framework (Hu et al., 2011). Thus, it is very likely that Na content significantly affects the electrical conductivity of amphiboles (**Figure 3**). When we compare our electrical conductivity data with prior results on amphibole-bearing samples, we found a strong correlation between the electrical conductivity and the Na_2O content, i.e., as the Na_2O content in the amphibole phase of the sample increases, the electrical conductivity is also enhanced (**Figure 3**). The activation enthalpy for our sample at lower temperatures i.e., in the solid-state is also much lower than that of the samples with lower Na content (**Figure 3**, **Table 2**).

The electrical conductivity of major mantle mineral phases (nominally anhydrous mineral (NAM) phases), including olivine (Gardés et al., 2014; Xu et al., 2000; Wang et al., 2006; Yoshino

et al., 2006, 2009; Dai et al., 2010; Dai and Karato, 2014a, b; Fei et al., 2020), pyroxene (Dai and Karato, 2009a), and garnet (Dai and Karato, 2009b) is lower than that of amphiboles or amphibole-bearing rocks (**Figure S4**). One exception is that the electrical conductivity of orthopyroxene is slightly higher than that of pure tremolite (Yang et al., 2012; Shen et al., 2020). However, trace amounts of water/hydrogen often have a significant impact on the electrical conductivity, because hydrogen atoms in NAMs occur as defects and are not structurally bonded (Karato, 1990; Wang et al., 2006). For example, the electrical conductivity of garnet with ~50 ppm of water is quite comparable to those of Na-rich amphiboles or amphibole-bearing rocks at mid-lithosphere temperatures. While the electrical conductivity of volumetrically dominant mantle phases at MLD conditions, i.e., olivine and pyroxene with ~50 ppm of water, is still lower than those of Na-rich amphiboles, but comparable with Na-poor amphiboles (**Figure S4**).

Discussions

To test whether mantle metasomatism could be a plausible cause for MLD, we selected a natural metasomatized rock sample that consists of ~87% diopside, ~9% tremolite, and ~ 3% albite. The electrical conductivity of the diopside is similar to that of orthopyroxene (Yang et al., 2011, 2012) and slightly higher than that of olivine (Gardés et al., 2014). The metasomatized cratonic mantle often contains <10% amphiboles. To recreate chemistry and modal abundances of mineral phases in the metasomatized mantle, recent experimental studies have demonstrated that 90 wt.% depleted mantle rock and 10 wt.% rhyolitic melts could generate 3.6% to 9.4% amphiboles over 2-3 GPa and 1223-1323 K (Saha et al., 2018). Thus, our selected metasomatized sample with ~9% amphibole is a good representative for the metasomatized cratonic mantle rock.

Owing to the low modal abundance of amphiboles in the metasomatized mantle, it is very unlikely that they are interconnected. However, amphibole-bearing xenoliths do suggest that amphiboles might be connected via veins (Ionov and Hofmann, 1995). In our experiment, the texture of the starting sample does not show any evidence for the interconnectivity of the amphibole (**Figure S1**). However, the SEM image of the sample after the electrical conductivity measurement shows that tremolite develops a texture that resembles discontinuous and locally interconnected thin veins that are near perpendicular to the electrodes (**Figure 2**). These thin veins are not inherent to the sample and very likely represent quenched aqueous fluids along the grain boundaries.

In the earlier electrical conductivity study on tremolite, the sample had little Na. In contrast, our sample assemblage contains Na-bearing tremolite and albite which is more representative of the metasomatized mantle rock in MLD. It is well known that tremolite and albite may form edenite amphiboles at higher pressures (Spear, 1981). Tremolite + tschermakite amphibole + albite could form pargasite amphibole at higher pressures (Bhadra and Bhattacharya, 2007). It is also well known that the most relevant phase of amphiboles stable at MLD conditions is pargasitic-edenitic amphiboles (Mandler and Grove, 2016; Saha et al., 2018), which translates to 3.4-4.4 wt.% Na_2O content in amphiboles (Saha et al., 2018). The even higher Na content in MLD indicates that the electrical conductivity is likely to be similar or higher than our electrical conductivity results. Such a high conductivity is very likely to cause a positive anomaly. This is however not detected by MT observations and thus puts severe constraints on metasomatism as a viable mechanism to explain MLD.

Implication

Our experimental electrical conductivity data can provide independent and important constraints on the debated mechanism of MLD, i.e., mantle metasomatism. To better evaluate the electrical conductivity of the metasomatized mantle, we used our results on the temperature dependence of the electrical conductivity of diopside-tremolite-albite rock and extrapolated to conditions relevant for MLD. We calculated the electrical conductivity vs. depth along a typical steady-state conductive geotherm of the cratonic lithosphere, with a surface heat flux of 45 mW/m^2 (Lee et al., 2011) (**Figure 4**). We extrapolated the electrical conductivity of the solid-state regime to MLD depths. To compare with pristine mantle free from any metasomatism, we determined electrical conductivity-depth profiles using a depleted peridotite composition consisting of ~48.5% olivine, ~41.5% orthopyroxene, ~9.1% garnet, and ~0.9% clinopyroxene. This mantle rock model is based on the average composition of the global cratonic xenoliths (Saha et al., 2018; Lee et al., 2011; Luguet et al., 2015; Maier et al., 2012; Pearson and Wittig, 2013). We also considered the effect of enhanced electrical conductivity due to hydrogen defects in NAMs. As we all know, cratons are stable which indicates cratons are rheologically stiff and often dry so that they resist being swept away by mantle convection. However, recent studies have shown that most of the cratonic lithospheric mantle is not as dry as assumed and can contain a small amount of water in NAMs such that it will not affect the overall rheological strength of the craton, i.e., it can sustain over geological times (Selway, 2019; Demouchy and Bolfan-Casanova, 2016; Griffin et al., 2009; Saal et al., 2002; Simons et al., 2002; Freitas and Manthilake, 2019). Thus, we considered two distinct cases for the unmetasomatized "background" mantle- (a) major mantle minerals are "dry" and (b) major mantle minerals are "wet" with an aggregate water content of 50 ppm (Saal et al., 2002; Simons et al., 2002; Freitas and Manthilake, 2019). We also considered the partition coefficients of water among these major mantle phases from earlier studies for the "wet" model

(Ardia et al., 2012; Férot and Bolfan-Casanova, 2012; Demouchy and Bolfan-Casanova, 2016; Mookherjee and Karato, 2010).

To estimate the electrical conductivity of the unmetasomatized "background" mantle, we used the generalized Archie's Law (Glover, 2010):

$$\sigma = \sum_i^n \sigma_i \phi_i^{m_i}, \quad (2)$$

where σ_i is the electrical conductivity of the i^{th} mineral phase (i=1,2,…,n), ϕ_i is the modal abundance of the i^{th} mineral phase, and m_i is the connectivity exponent of the i^{th} mineral phase which is inversely related to the physical connectivity of mineral phase. We used the connectivity exponent m_i= 1.3 for the i^{th} phase comprising ≥20% of the whole rock, m_i= 2 for the phase comprising 10-20%, and m_i= 3 for the phase comprising <10% (Selway, 2019). For an ideal connection, m= 1.

We calculated the electrical conductivity of two distinct lithologies by combining the electrical conductivity of metasomatized rock, i.e., our study, with (a) "dry background" mantle and (b) "wet background" mantle. We compared the predicted electrical conductivity-depth profiles with available MT data (Yang et al., 2015) near two distinct seismic stations JFWS and EYMN located in the northern US (Selway, 2019). These two stations have reported MLDs at depths of 59 km and 94 km, respectively (Abt et al., 2010). To explain the MT observations, we varied the proportion of the depleted peridotite rock and the metasomatized rock.

We found that at the MLD depth, i.e., ~60-95 km in the northern US, the conductivity of our metasomatized rock is 3.1-4.6 orders of magnitude greater than the "dry" depleted mantle and 1.6-2.4 orders of magnitude greater than the "wet" depleted mantle with 50 ppm of water (**Figure 4**). The difference between the electrical conductivity of the "dry" and "wet" depleted mantle is due to the effect of extrinsic hydrogen defects. We also found that if the sub cratonic mantle is

"dry", the lower bound of the observed MT profile could be explained by ~7% of partial metasomatism. This means ~0.6% amphiboles in the bulk rock. While the upper bound could be explained by partial metasomatism not exceeding 17%, which is equivalent to ~1.5% amphibole in the bulk rock. In the "wet" mantle, we noted that without the effect of mantle metasomatism, it is already sufficient to explain the observed MT profiles. And the upper bound of the MT profiles could be explained <14% of partial metasomatism, i.e., <1.3% amphibole in the bulk rock (**Figure 4**). However, ~1.5% amphibole in the bulk rock could only reduce the shear seismic wave velocity by ~0.4-0.5% at MLD depths (Saha et al., 2021; Peng and Mookherjee, 2020), while a 2-6% reduction in the shear seismic wave velocity has been observed in most MLD regions (Rychert and Shearer, 2009; Romanowicz, 2009; Abt et al., 2010; Fischer et al., 2010). Hence, our results do indicate that irrespective of whether the sub-cratonic mantle is "dry" or "wet", the presence of Na-rich amphibole-bearing rock, or mantle metasomatism cannot explain the shear seismic wave velocity and electrical conductivity of MLD simultaneously.

Acknowledgments

The authors thank the Associate Editor Prof. Zhicheng Jing and the two reviewers Prof. Lidong Dai and Dr. Hongzhan Fei for their constructive criticism that enhanced the clarity of the article. Y.P. and M.M. acknowledge NSF funding EAR 1763215 and 1753125. G.M. acknowledges funding from the INSU-CNRS. This research was also financed by the French Government Laboratory of Excellence initiative n°ANR-10-LABX-0006, the Région Auvergne, and the European Regional Development Fund (ClerVolc contribution number 472).

References

Abt, D.L., Fischer, K.M., French, S.W., Ford, H.A., Yuan, H., and Romanowicz, B. (2010) North American lithospheric discontinuity structure imaged by P_S and S_P receiver functions. Journal of Geophysical Research: Solid Earth, 115, B09301. https://doi.org/10.1029/2009JB006914

Ardia, P., Hirschmann, M.M., Withers, A.C., and Tenner, T.J. (2012) H_2O storage capacity of olivine at 5–8 GPa and consequences for dehydration partial melting of the upper mantle. Earth and Planetary Science Letters, 345, 104-116. https://doi.org/10.1016/j.epsl.2012.05.038

Bhadra, S., and Bhattacharya, A. (2007) The barometer tremolite+ tschermackite+ 2 albite= 2 pargasite+ 8 quartz: Constraints from experimental data at unit silica activity, with application to garnet-free natural assemblages. American Mineralogist, 92, 491-502. https://doi.org/10.2138/am.2007.2067

Dai, L., and Karato, S.-I. (2009a) Electrical conductivity of orthopyroxene: Implications for the water content of the asthenosphere. Proceedings of the Japan Academy, Series B, 85, 466-475. https://doi.org/10.2183/pjab.85.466

Dai, L., and Karato, S.-I. (2009b) Electrical conductivity of pyrope-rich garnet at high temperature and high pressure. Physics of the Earth and Planetary Interiors, 176, 83-88. https://doi.org/10.1016/j.pepi.2009.04.002

Dai, L., and Karato, S.-I. (2014a) The effect of pressure on the electrical conductivity of olivine under the hydrogen-rich conditions. Physics of the earth and Planetary Interiors, 232, 51-56. https://doi.org/10.1016/j.pepi.2014.03.010

Dai, L., and Karato, S.-I. (2014b) Influence of oxygen fugacity on the electrical conductivity of hydrous olivine: Implications for the mechanism of conduction. Physics of the Earth and Planetary Interiors, 232, 57-60. https://doi.org/10.1016/j.pepi.2014.04.003

Dai, L., Li, H., Li, C., Hu, H., and Shan, S. (2010) The electrical conductivity of dry polycrystalline olivine compacts at high temperatures and pressures. Mineralogical Magazine, 74, 849-857. https://doi.org/10.1180/minmag.2010.074.5.849

Demouchy, S., and Bolfan-Casanova, N. (2016) Distribution and transport of hydrogen in the lithospheric mantle: A review. Lithos, 240, 402-425. https://doi.org/10.1016/j.lithos.2015.11.012

Fei, H., Druzhbin, D., and Katsura, T. (2020) The effect of water on ionic conductivity in olivine. Journal of Geophysical Research: Solid Earth, 125, e2019JB019313. https://doi.org/10.1029/2019JB019313

Férot, A., and Bolfan-Casanova, N. (2012) Water storage capacity in olivine and pyroxene to 14 GPa: Implications for the water content of the Earth's upper mantle and nature of seismic discontinuities. Earth and Planetary Science Letters, 349, 218-230. https://doi.org/10.1016/j.epsl.2012.06.022

Fischer, K.M., Ford, H.A., Abt, D.L., and Rychert, C.A. (2010) The lithosphere-asthenosphere boundary. Annual Review of Earth and Planetary Science, 38, 551-575. https://doi.org/10.1146/annurev-earth-040809-152438

Ford, H.A., Long, M.D., and Wirth, E.A. (2016) Midlithospheric discontinuities and complex anisotropic layering in the mantle lithosphere beneath the Wyoming and Superior Provinces. Journal of Geophysical Research: Solid Earth, 121, 6675-6697. https://doi.org/10.1002/2016JB012978

384 Freitas, D., and Manthilake, G. (2019) Electrical conductivity of hydrous silicate melts:
385 Implications for the bottom-up hydration of Earth's upper mantle. Earth and Planetary
386 Science Letters, 523, 115712. https://doi.org/10.1016/j.epsl.2019.115712
387 Gardés, E., Gaillard, F., and Tarits, P. (2014) Toward a unified hydrous olivine electrical
388 conductivity law. Geochemistry, Geophysics, Geosystems, 15, 4984-5000.
389 https://doi.org/10.1002/2014GC005496
390 Glover, P.W.J. (2010) A generalized Archie's law for n phases. Geophysics, 75, E247-E265.
391 https://doi.org/10.1190/1.3509781
392 Griffin, W.L., O'Reilly, S.Y., Afonso, J.C., and Begg, G.C. (2009) The composition and
393 evolution of lithospheric mantle: a re-evaluation and its tectonic implications. Journal of
394 Petrology, 50, 1185-1204. https://doi.org/10.1093/petrology/egn033
395 Hansen, S.M., Dueker, K., and Schmandt, B. (2015) Thermal classification of lithospheric
396 discontinuities beneath USArray. Earth and Planetary Science Letters, 431, 36-47.
397 https://doi.org/10.1016/j.epsl.2015.09.009
398 He, Y., Sun, Y., Lu, X., Gao, J., Li, H., and Li, H. (2016) First-principles prediction of fast
399 migration channels of potassium ions in $KAlSi_3O_8$ hollandite: Implications for high
400 conductivity anomalies in subduction zones. Geophysical Research Letters, 43, 6228-6233.
401 https://doi.org/10.1002/2016GL069084
402 Hu, H., Dai, L., Li, H., Sun, W., and Li, B. (2018) Effect of dehydrogenation on the electrical
403 conductivity of Fe-bearing amphibole: Implications for high conductivity anomalies in
404 subduction zones and continental crust. Earth and Planetary Science Letters, 498, 27-37.
405 https://doi.org/10.1016/j.epsl.2018.06.003

406 Hu, H., Li, H., Dai, L., Shan, S., and Zhu, C. (2011) Electrical conductivity of albite at high
407 temperatures and high pressures. American Mineralogist, 96, 1821-1827.
408 https://doi.org/10.2138/am.2011.3796
409 Ionov, D.A., and Hofmann, A.W. (1995) Nb-Ta-rich mantle amphiboles and micas: Implications
410 for subduction-related metasomatic trace element fractionations. Earth and Planetary
411 Science Letters, 131, 341-356. https://doi.org/10.1016/0012-821X(95)00037-D
412 Karato, S.-I. (1990) The role of hydrogen in the electrical conductivity of the upper mantle.
413 Nature, 347, 272-273. https://doi.org/10.1038/347272a0
414 Karato, S.-I., and Park, J. (2019) On the origin of the upper mantle seismic discontinuities. In H.
415 Yuan and B. Romanovicz, Eds., Lithospheric Discontinuities, Geophysical Monograph
416 Series (Vol. 239, p. 5-34). Washington, DC: American Geophysical Union.
417 https://doi.org/10.1002/9781119249740.ch1
418 Karato, S.-I., Olugboji, T., and Park, J. (2015) Mechanisms and geologic significance of the mid-
419 lithosphere discontinuity in the continents. Nature Geoscience, 8, 509-514.
420 https://doi.org/10.1038/ngeo2462
421 Lafuente, B., Downs, R.T., Yang, H., and Stone, N. (2015) The power of databases: the RRUFF
422 project. In T. Armbruster and R.M. Danisi, Eds., Highlights in mineralogical
423 crystallography (p. 1-30). Berlin, Germany: Walter de Gruyter.
424 https://doi.org/10.1515/9783110417104-003
425 Lee, C.-T.A., Luffi, P., and Chin, E.J. (2011) Building and destroying continental mantle.
426 Annual Review of Earth and Planetary Sciences, 39, 59-90.
427 https://doi.org/10.1146/annurev-earth-040610-133505

Luguet, A., Behrens, M., Pearson, D.G., König, S., and Herwartz, D. (2015) Significance of the whole rock Re-Os ages in cryptically and modally metasomatised cratonic peridotites: Constraints from HSE–Se–Te systematics. Geochimica et Cosmochimica Acta, 164, 441-463. https://doi.org/10.1016/j.gca.2015.06.016

Maier, W.D., Peltonen, P., McDonald, I., Barnes, S.J., Barnes, S.J., Hatton, C., and Viljoen, F. (2012) The concentration of platinum-group elements and gold in southern African and Karelian kimberlite-hosted mantle xenoliths: implications for the noble metal content of the Earth's mantle. Chemical Geology, 302, 119-135. https://doi.org/10.1016/j.chemgeo.2011.06.014

Mandler, B.E., and Grove, T.L. (2016) Controls on the stability and composition of amphibole in the Earth's mantle. Contributions to Mineralogy and Petrology, 171, 68. https://doi.org/10.1007/s00410-016-1281-5

Manthilake, G., Bolfan-Casanova, N., Novella, D., Mookherjee, M., and Andrault, D. (2016) Dehydration of chlorite explains anomalously high electrical conductivity in the mantle wedges. Science advances, 2, e1501631. https://doi.org/10.1126/sciadv.1501631

Manthilake, G., Mookherjee, M., and Miyajima, N. (2021) Insights on the deep carbon cycle from the electrical conductivity of carbon-bearing aqueous fluids. Scientific Reports. https://doi.org/10.1038/s41598-021-82174-8

Manthilake, G., Mookherjee, M., Bolfan-Casanova, N., and Andrault, D. (2015) Electrical conductivity of lawsonite and dehydrating fluids at high pressures and temperatures. Geophysical Research Letters, 42, 7398-7405. https://doi.org/10.1002/2015GL064804

Manthilake, G., Schiavi, F., Zhao, C., Mookherjee, M., Bouhifd, M.A., and Jouffret, L. (2020) The Electrical Conductivity of Liebermannite: Implications for Water Transport Into the

Earth's Lower Mantle. Journal of Geophysical Research: Solid Earth, 125, e2020JB020094. https://doi.org/10.1029/2020JB020094

Meqbel, N.M., Egbert, G.D., Wannamaker, P.E., Kelbert, A., and Schultz, A. (2014) Deep electrical resistivity structure of the northwestern US derived from 3-D inversion of USArray magnetotelluric data. Earth and Planetary Science Letters, 402, 290-304. https://doi.org/10.1016/j.epsl.2013.12.026.

Mookherjee, M., and Karato, S.-I. (2010) Solubility of water in pyrope-rich garnet at high pressures and temperature. Geophysical Research Letters, 37, L03310. https://doi.org/10.1029/2009GL041289

Pearson, D.G., and Wittig, N. (2013) The formation and evolution of cratonic mantle lithosphere: Evidence from mantle xenoliths. In R.W. Carlson and H.D. Holland, Eds., The mantle and core, Treatise on Geochemistry (Vol. 3, p. 225-292). Oxford, UK: Elsevier.

Peng, Y., and Mookherjee, M. (2020) Thermoelasticity of tremolite amphibole: Geophysical implications. American Mineralogist, 105, 904-916. https://doi.org/10.2138/am-2020-7189

Pommier, A., and Evans, R.L. (2017) Constraints on fluids in subduction zones from electromagnetic data. Geosphere, 13, 1026-1041. https://doi.org/10.1130/GES01473.1

Pommier, A., Williams, Q., Evans, R.L., Pal, I., and Zhang, Z. (2019) Electrical Investigation of Natural Lawsonite and Application to Subduction Contexts. Journal of Geophysical Research: Solid Earth, 124, 1430-1442. https://doi.org/10.1029/2018JB016899

Rader, E., Emry, E., Schmerr, N., Frost, D., Cheng, C., Menard, J., Yu, C., and Geist, D. (2015) Characterization and petrological constraints of the midlithospheric discontinuity. Geochemistry, Geophysics, Geosystems, 16, 3484-3504. https://doi.org/10.1002/2015GC005943.

474 Romanowicz, B. (2009) The thickness of tectonic plates. Science, 324, 474-476.
475 https://doi.org/10.1126/science.1172879
476 Rychert, C.A., and Shearer, P.M. (2009) A global view of the lithosphere-asthenosphere
477 boundary. Science, 324, 495-498. https://doi.org/10.1126/science.1169754
478 Saal, A.E., Hauri, E.H., Langmuir, C.H., and Perfit, M.R. (2002) Vapour undersaturation in
479 primitive mid-ocean-ridge basalt and the volatile content of Earth's upper mantle. Nature,
480 419, 451-455. https://doi.org/10.1038/nature01073
481 Saha, S., Dasgupta, R., and Tsuno, K. (2018) High pressure phase relations of a depleted
482 peridotite fluxed by CO_2-H_2O-bearing siliceous melts and the origin of mid-lithospheric
483 discontinuity. Geochemistry, Geophysics, Geosystems, 19, 595-620.
484 https://doi.org/10.1002/2017GC007233
485 Saha, S., Peng, Y., Dasgupta, R., Mookherjee, M., and Fischer, K.M. (2021) Assessing the
486 presence of volatile-bearing mineral phases in the cratonic mantle as a possible cause of
487 mid-lithospheric discontinuities. Earth and Planetary Science Letters, 553, 116602.
488 https://doi.org/10.1016/j.epsl.2020.116602
489 Savage, B., and Silver, P.G. (2008) Evidence for a compositional boundary within the
490 lithospheric mantle beneath the Kalahari craton from S receiver functions. Earth and
491 Planetary Science Letters, 272, 600-609. https://doi.org/10.1016/j.epsl.2008.05.026
492 Schneider, C.A., Rasband, W.S., and Eliceiri, K.W. (2012) NIH Image to ImageJ: 25 years of
493 image analysis. Nature Methods, 9, 671-675. https://doi.org/10.1038/nmeth.2089
494 Selway, K. (2019) Electrical discontinuities in the continental lithosphere imaged with
495 magnetotellurics. In H. Yuan and B. Romanovicz, Eds., Lithospheric Discontinuities,

Geophysical Monograph Series (Vol. 239, p. 89-109). Washington, DC: American Geophysical Union. https://doi.org/10.1002/9781119249740.ch5

Selway, K., Ford, H., and Kelemen, P. (2015) The seismic mid lithosphere discontinuity. Earth and Planetary Science Letters, 414, 45-57. https://doi.org/10.1016/j.epsl.2014.12.029

Shen, K., Wang, D., and Liu, T. (2020) Electrical conductivity of tremolite under high temperature and pressure: implications for the high-conductivity anomalies in the Earth and Venus. Contributions to Mineralogy and Petrology, 175, 52. https://doi.org/10.1007/s00410-020-01688-y

Simons, K., Dixon, J., Schilling, J.G., Kingsley, R., and Poreda, R. (2002) Volatiles in basaltic glasses from the Easter-Salas y Gomez Seamount Chain and Easter Microplate: Implications for geochemical cycling of volatile elements. Geochemistry, Geophysics, Geosystems, 3, 1-29. https://doi.org/10.1029/2001GC000173

Sodoudi, F., Yuan, X., Kind, R., Lebedev, S., Adam, J.M.C., Kästle, E., and Tilmann, F. (2013) Seismic evidence for stratification in composition and anisotropic fabric within the thick lithosphere of Kalahari Craton. Geochemistry, Geophysics, Geosystems, 14, 5393-5412. https://doi.org/10.1002/2013GC004955

Spear, F.S. (1981) Amphibole-plagioclase equilibria: an empirical model for the relation albite+ tremolite= edenite+ 4 quartz. Contributions to Mineralogy and Petrology, 77, 355-364. https://doi.org/10.1007/BF00371564

Thybo, H. (2006) The heterogeneous upper mantle low velocity zone. Tectonophysics, 416, 53-79. https://doi.org/10.1016/j.tecto.2005.11.021

517 Wang, D., Guo, Y., Yu, Y., and Karato, S.-I. (2012) Electrical conductivity of amphibole-
518 bearing rocks: Influence of dehydration. Contributions to Mineralogy and Petrology, 164,
519 17-25, https://doi.org/10.1007/s00410-012-0722-z
520 Wang, D., Mookherjee, M., Xu, Y., and Karato, S.-I. (2006) The effect of water on the electrical
521 conductivity of olivine. Nature, 443, 977-980. https://doi.org/10.1038/nature05256
522 Wirth, E.A., and Long, M.D. (2014) A contrast in anisotropy across mid-lithospheric
523 discontinuities beneath the central United States-A relic of craton formation. Geology, 42,
524 851-854. https://doi.org/10.1130/G35804.1
525 Xu, Y., Shankland, T. J., and Duba, A. G. (2000) Pressure effect on electrical conductivity of
526 mantle olivine. Physics of the Earth and Planetary Interiors, 118, 149-161.
527 https://doi.org/10.1016/S0031-9201(99)00135-1
528 Yang, B., Egbert, G.D., Kelbert, A., and Meqbel, N.M. (2015) Three-dimensional electrical
529 resistivity of the north-central USA from EarthScope long period magnetotelluric data.
530 Earth and Planetary Science Letters, 422, 87-93. https://doi.org/10.1016/j.epsl.2015.04.006
531 Yang, X., Keppler, H., McCammon, C., and Ni, H. (2012) Electrical conductivity of
532 orthopyroxene and plagioclase in the lower crust. Contributions to Mineralogy and
533 Petrology, 163, 33-48. https://doi.org/10.1007/s00410-011-0657-9
534 Yang, X., Keppler, H., McCammon, C., Ni, H., Xia, Q., and Fan, Q. (2011) Effect of water on
535 the electrical conductivity of lower crustal clinopyroxene. Journal of Geophysical
536 Research: Solid Earth, 116, B04208. https://doi.org/10.1029/2010JB008010
537 Yoshino, T., Matsuzaki, T., Shatskiy, A., and Katsura, T. (2009) The effect of water on the
538 electrical conductivity of olivine aggregates and its implications for the electrical structure

of the upper mantle. Earth and Planetary Science Letters, 288, 291-300. https://doi.org/10.1016/j.epsl.2009.09.032

Yoshino, T., Matsuzaki, T., Yamashita, S., and Katsura, T. (2006) Hydrous olivine unable to account for conductivity anomaly at the top of the asthenosphere. Nature, 443, 973-976. https://doi.org/10.1038/nature05223

Yuan, H., Romanowicz, B. (2010) Lithospheric layering in the North American craton. Nature, 466, 1063-1068. https://doi.org/10.1038/nature09332

Figures caption

Figure 1. Raman spectrum of the natural metasomatized rock sample containing diopside, tremolite, and albite (Di-Tr-Ab) (red) at ambient conditions. It is compared with the reference Raman spectra for diopside (Di) (RRUFF ID: R040109; black), tremolite (Tr) (RRUFF ID: R040009; blue), and albite (Ab) (RRUFF ID: R040068; green) (Lafuente et al., 2015).

Figure 2. (**a**) Electrical conductivity of diopside-tremolite-albite sample as a function of reciprocal temperature. The sample was subjected to several heating-cooling cycles. The lines represent Arrhenius fits to the data, except for the first heating-cooling cycle. The colored numbers indicate the activation enthalpy associated with each regime, i.e., solid-state conduction and partial dehydration. (**b**) SEM image of the sample after the electrical conductivity experiment. The mineral phases are labeled. Locally interconnected thin bands of tremolite phase are noted. Abbreviation: Di- diopside, Tr- tremolite, Ab- albite, and Fls- fluids.

Figure 3. Plot of electrical conductivity of the diopside-tremolite-albite (Di-Tr-Ab) sample as a function of reciprocal temperature. The colored numbers indicate the Na_2O content in the amphibole phase of the samples and the total FeO content of the samples. Note: the filled red symbols- data from this study; the bold red lines- Arrhenius fit to data from this study; the dark blue line- hornblende-actinolite-bearing hornblendite (Hbl-Act) (W12: Wang et al., 2012); the intermediate blue line- plagioclase-hornblende-bearing hornblendite parallel to the lineation within the sample (Pl-Hbl//); the light blue line- plagioclase-hornblende-bearing hornblendite perpendicular to the lineation within the sample (Pl-Hbl⊥); the orange line- clinopyroxene (Cpx) (Y11: Yang et al., 2011); the purple line- tremolite (Tr) (S20: Shen et al., 2020); and the green line- amphibole (Amp) (H18: Hu et al., 2018). *We note an unreasonable high CaO content ~20.43 wt.% in the amphibole sample (Hu et al., 2018). This might indicate that the amphibole sample is not representative of the lithosphere. The relevant CaO content for amphiboles that are likely to be stable in the metasomatized mantle ranges between 9.2-12.6 wt.% (Saha et al., 2021).

Figure 4. The conductivity-depth profile of the diopside-tremolite-albite sample (Di-Tr-Ab) (green lines) and predicted conductivity-depth profiles of the (**a**) "dry" and (**b**) "wet" (50 ppm of water) depleted peridotite (DP) based on the generalized Archie's Law. The lighter red and blue lines are the bulk conductivity of the mixed model. For example, DP+7% MR means the bulk rock consists of 93% depleted peridotite (DP) and 7% of our metasomatized rock (MR), i.e., the diopside-tremolite-albite sample. The dashed lines indicate the conductivity-depth profiles from the three-dimensional MT models near seismic stations JFWS and EYMN in the northern US (Yang et al., 2015). The cyan shaded area shows the depth range of MLDs reported at the two seismic stations (Abt et al., 2010).

Table 1. Chemical composition (wt.%) of mineral phases in the sample assemblage determined by EPMA before and after the electrical conductivity measurements. The chemical composition of each phase is slightly modified after the experiment.

Sample	SiO_2	MgO	CaO	Al_2O_3	Na_2O	K_2O	FeO	TiO_2	Cr_2O_3	NiO	MnO	Total	Modal abundance
Before													
Di	$(Mg_{1.02}Ca_{0.85}Na_{0.09}Al_{0.06})(Si_{1.99}Al_{0.01})O_6$												87.5%
	55.58	19.10	22.03	1.62	1.25	0.00	0.12	0.02	0.04	0.09	-	99.86	
Tr	$(Na_{0.19}K_{0.03})(Ca_{1.61}Na_{0.39})(Mg_{5.09}Fe_{0.02}Ti_{0.01})(Si_{7.75}Al_{0.29})O_{22}(OH)_2$												9.1%
	58.27	25.68	11.28	1.83	2.24	0.17	0.17	0.14	0.04	0.04	-	99.87	
Ab	$(Na_{1.09}K_{0.01})Al_{1.03}Si_{2.94}O_8$												3.4%
	66.70	0.37	0.07	19.77	12.79	0.11	0.04	0.03	0.02	0.09	-	99.97	
After													
Di	$(Ca_{0.96}Na_{0.04})(Mg_{0.95}Al_{0.04})Si_{2.00}O_6$												87.2%
	55.94	17.76	24.95	0.87	0.54	0.00	0.18	0.03	0.04	-	0.17	100.49	
Tr	$(Na_{0.38}K_{0.05})(Ca_{1.73}Na_{0.27})(Mg_{4.69}Al_{0.17}Ti_{0.06}Fe_{0.03}Mn_{0.02})(Si_{7.61}Al_{0.39})O_{22}(OH)_2$												9.1%
	57.15	23.24	12.29	2.50	1.69	0.19	0.26	0.34	0.03	-	0.18	97.89	
Ab	$(Na_{0.96}K_{0.01}Mg_{0.01}Ca_{0.01})Al_{1.01}Si_{2.99}O_8$												3.4%
	69.32	0.03	0.32	19.88	11.41	0.16	0.01	0.00	0.00	-	0.01	101.15	
Loss													0.3%

Note: abbreviation: Di- diopside, Tr- tremolite, and Ab- albite.

Table 2. Arrhenius fit parameters of the diopside-tremolite sample in this study and previous studies with experimental pressure and temperature conditions. The numbers in parentheses is the error of the last digit with one standard deviation.

Mineral phase	P (GPa)	T_1 (K)	Logσ_{01} (S/m)	ΔH_1 (eV)	T_2 (K)	Logσ_{02} (S/m)	ΔH_2 (eV)	T_3 (K)	Logσ_{03} (S/m)	ΔH_3 (eV)	T_4 (K)	Logσ_{04} (S/m)	ΔH_4 (eV)	Reference
Di-Tr-Ab	3.0	450-700	-0.59(3)	0.188(3)	775-1000	1.4(2)	0.48(3)	-	-	-	-	-	-	This study
Hbl-Act	0.5	420-736	2.03(9)	0.69(2)	760-824	24(2)	3.9(4)	-	-	-	-	-	-	Wang et al., 2012
Pl+Hbl(⊥)	1.0	443-824	1.18(7)	0.68(1)	840-900	18.0(7)	3.5(2)	-	-	-	-	-	-	Wang et al., 2012
Pl+Hbl(//)	1.0	395-771	1.49(7)	0.66(1)	797-857	18(2)	3.3(4)	-	-	-	-	-	-	Wang et al., 2012
Tr	2.0	648-898	-0.8(2)	0.75(3)	923-998	5.0(9)	1.7(2)	1023-1123	-1(1)	0.5(2)	1148-1373	14.2(6)	3.8(2)	Shen et al., 2020
Cpx	1.2	773-1273	2.2(3)	1.06(5)	-	-	-	-	-	-	-	-	-	Yang et al., 2011
Pl	1.2	773-1273	4.1(3)	1.67(6)	-	-	-	-	-	-	-	-	-	Yang et al., 2012
Amp*	2.0	623-873	2.08	0.81	923-1173	1.88	0.68	-	-	-	-	-	-	Hu et al., 2018

Note: abbreviation: Di- diopside, Tr- tremolite, Ab- albite, Hbl- hornblende, Act- actinolite, Pl- plagioclase, Cpx- clinopyroxene, and Amp- amphibole. *We note an unreasonable high CaO content ~20.43 wt.% in the amphibole sample (Hu et al., 2018). This might indicate that the amphibole sample is not representative of the lithosphere. The relevant CaO content for amphiboles that are likely to be stable in the metasomatized mantle ranges between 9.2-12.6 wt.% (Saha et al., 2021).

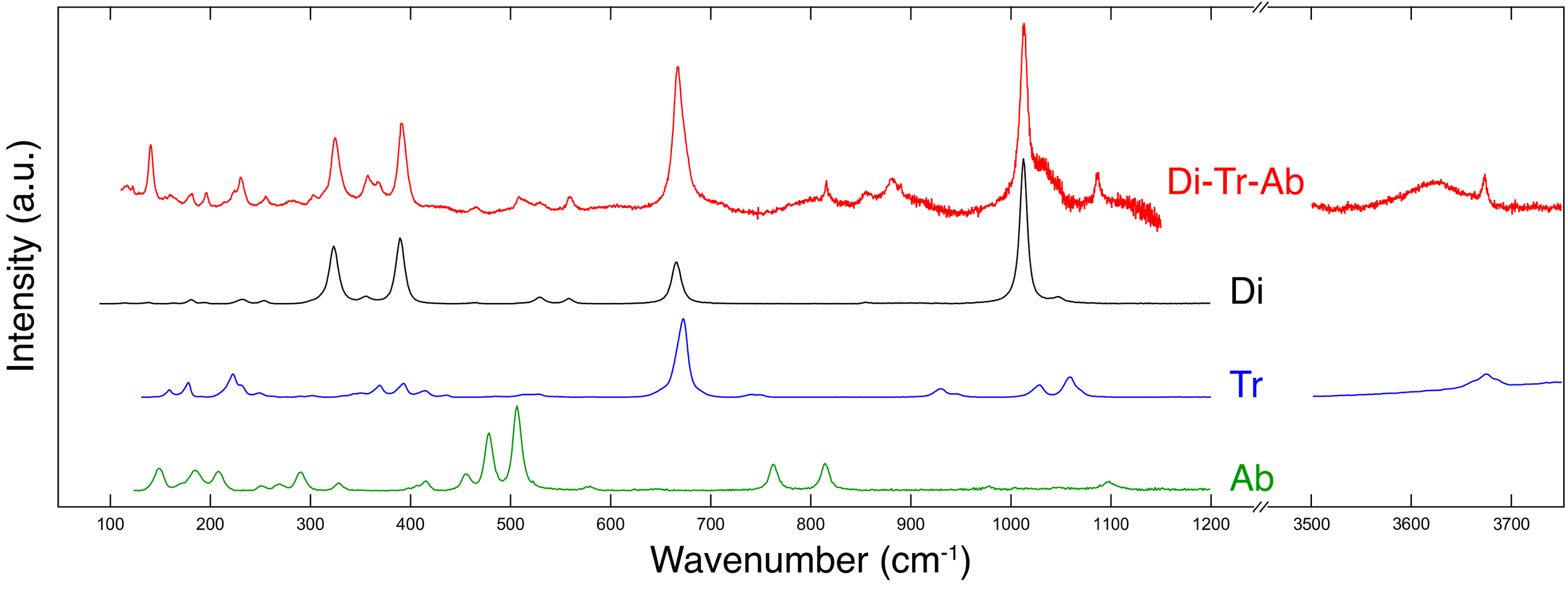
Intensity (a.u.)
Di-Tr-Ab
Di
Tr
Ab
100
200
300
400
500
600
700
800
900
1000
1100
1200
3500
3600
3700
Wavenumber (cm-1)

Figure 1

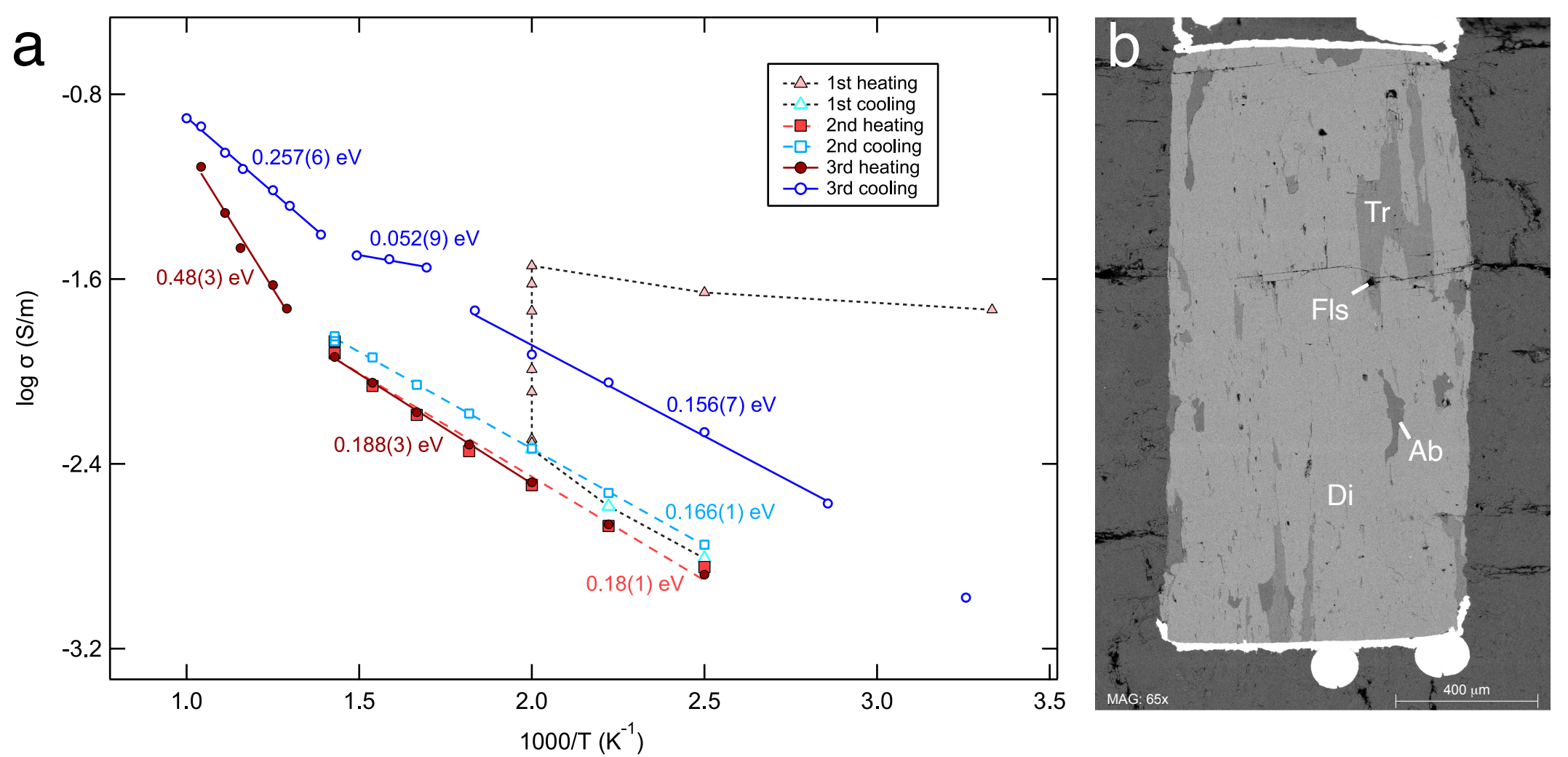
a
-0.8
-1.6
-2.4
-3.2
log σ (S/m)
1.0
1.5
2.0
2.5
3.0
3.5
1000/T (K-1)
1st heating
1st cooling
2nd heating
2nd cooling
3rd heating
3rd cooling
0.257(6) eV
0.052(9) eV
0.48(3) eV
0.156(7) eV
0.188(3) eV
0.166(1) eV
0.18(1) eV
b
Tr
Fls
Ab
Di
MAG: 65x
400 µm

Figure 2

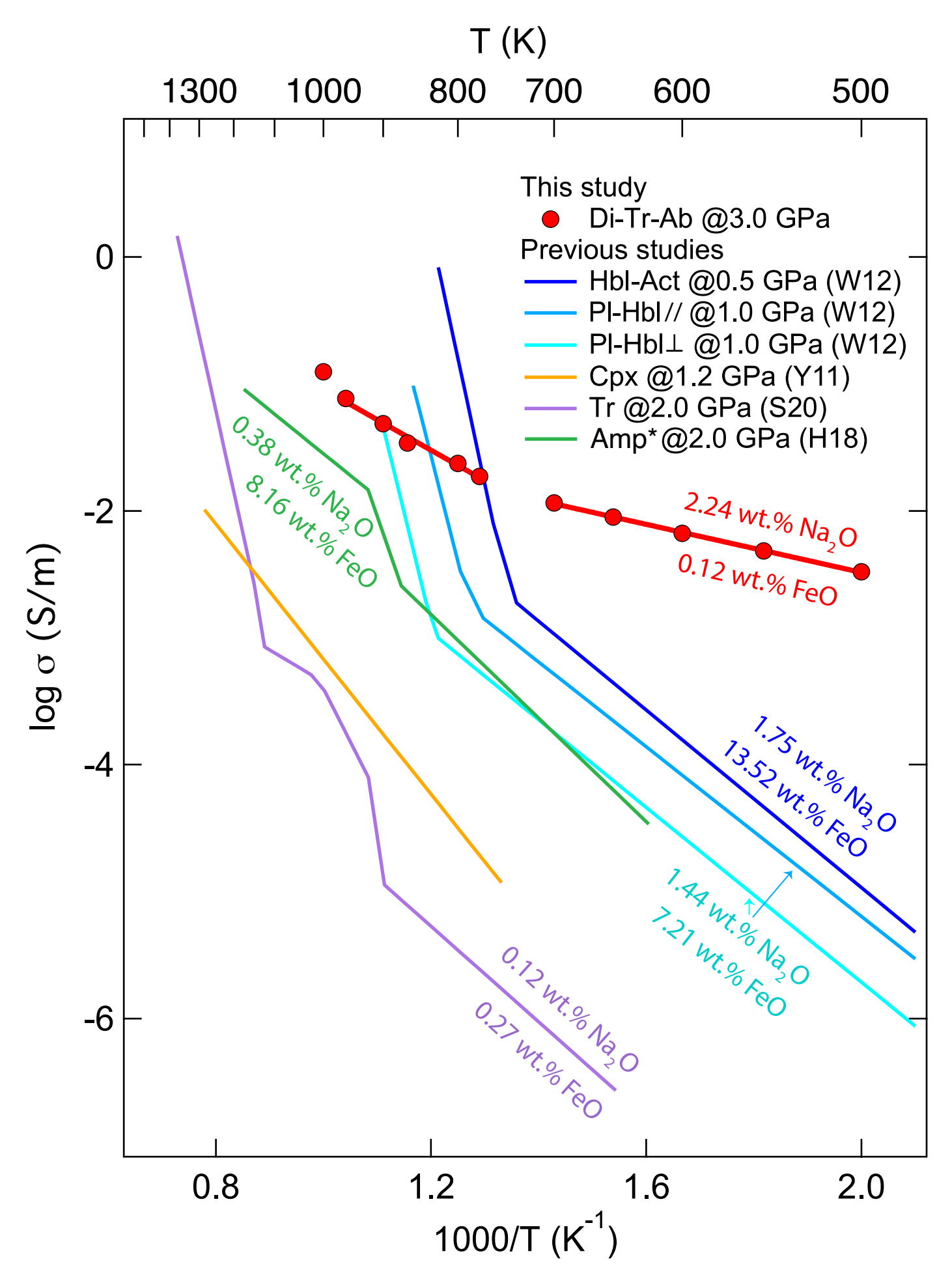
T (K)
1300
1000
800
700
600
500
This study
Di-Tr-Ab @3.0 GPa
Previous studies
Hbl-Act @0.5 GPa (W12)
Pl-Hbl// @1.0 GPa (W12)
Pl-Hbl⊥ @1.0 GPa (W12)
Cpx @1.2 GPa (Y11)
Tr @2.0 GPa (S20)
Amp*@2.0 GPa (H18)
0.38 wt.% Na2O
8.16 wt.% FeO
2.24 wt.% Na2O
0.12 wt.% FeO
1.75 wt.% Na2O
13.52 wt.% FeO
1.44 wt.% Na2O
7.21 wt.% FeO
0.12 wt.% Na2O
0.27 wt.% FeO
log σ (S/m)
0
-2
-4
-6
0.8
1.2
1.6
2.0
1000/T (K-1)

Figure 3

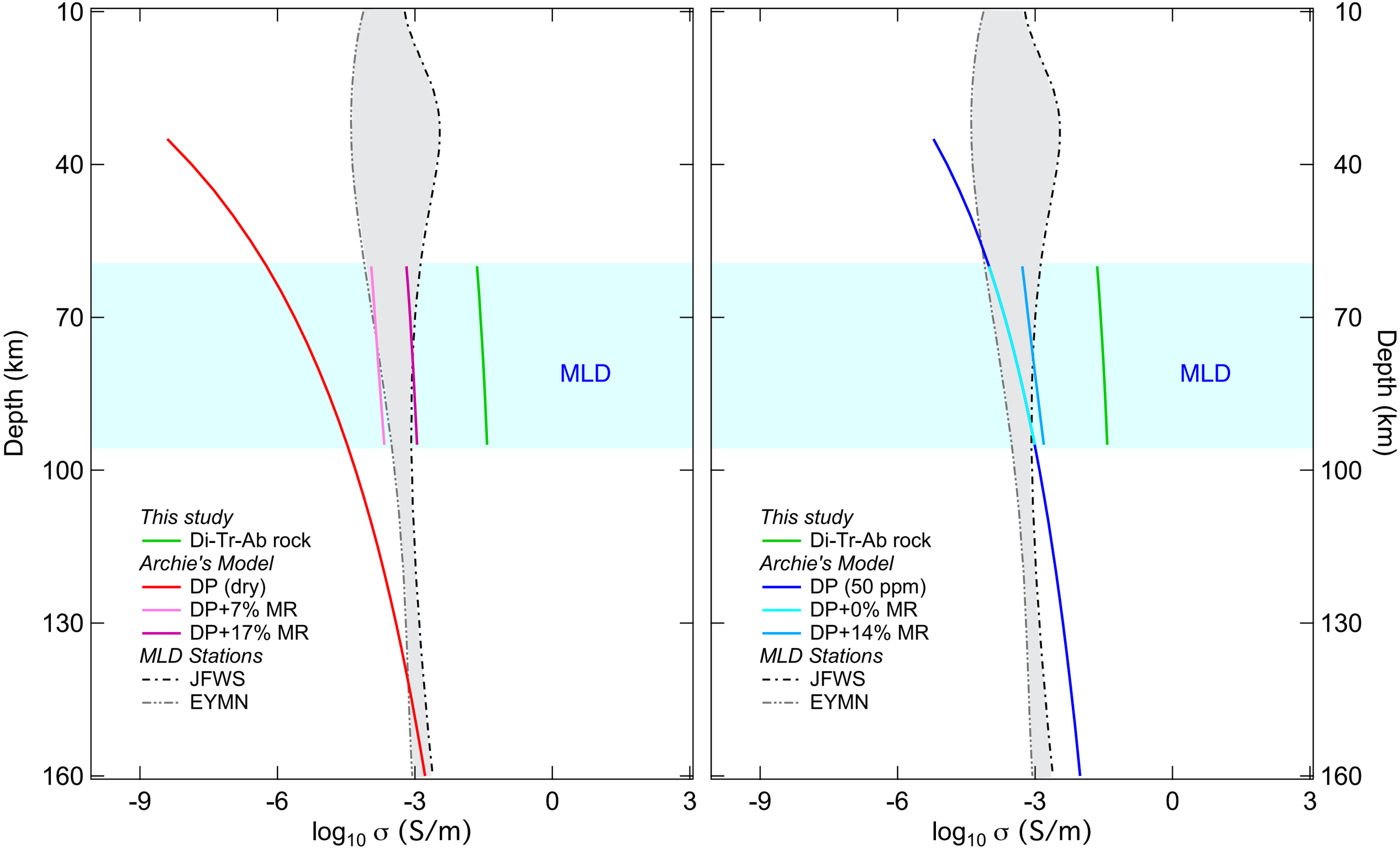
10
40
70
100
130
160
Depth (km)
MLD
This study
Di-Tr-Ab rock
Archie's Model
DP (dry)
DP+7% MR
DP+17% MR
MLD Stations
JFWS
EYMN
-9
-6
-3
0
3
log10 σ (S/m)
10
40
70
100
130
160
Depth (km)
MLD
This study
Di-Tr-Ab rock
Archie's Model
DP (50 ppm)
DP+0% MR
DP+14% MR
MLD Stations
JFWS
EYMN
-9
-6
-3
0
3
log10 σ (S/m)

Figure 4

Supporting Information

Electrical conductivity of metasomatized lithology in subcontinental lithosphere

Ye Peng[1*], Geeth Manthilake[2], and Mainak Mookherjee[1]

[1]Earth Materials Laboratory, Department of Earth, Ocean and Atmospheric Sciences, Florida State University, Tallahassee, FL, 32306 USA.

[2]Laboratoire Magmas et Volcans, CNRS, IRD, OPGC, Université Clermont Auvergne, Clermont-Ferrand, 63000 France.

*Corresponding author: Ye Peng (yp16b@my.fsu.edu)

Contents of this file

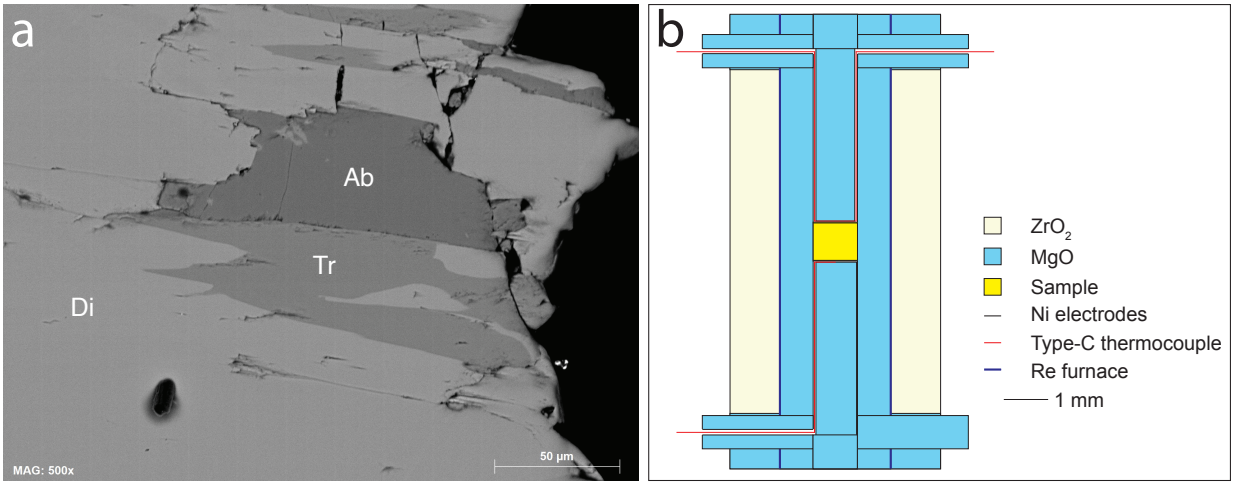

Figure S1. (**a**) SEM image of the diopside-tremolite-albite sample before the experiment. The mineral phases are labeled. Abbreviation: Di- diopside, Tr- tremolite, and Ab- albite. (**b**) Cross-section of the sample assembly for high-pressure and high-temperature electrical conductivity measurements.

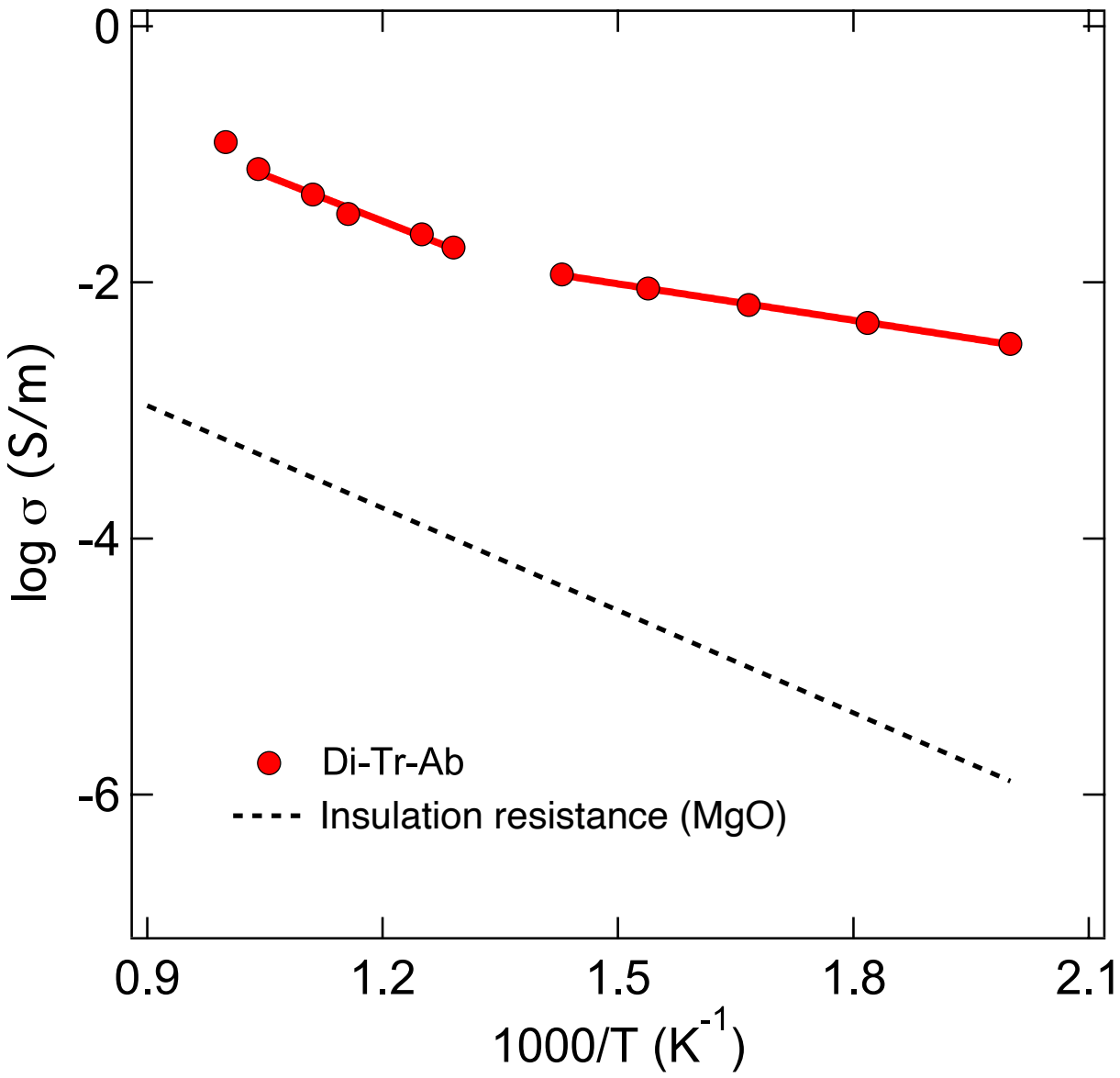

Figure S2. Comparison between the electrical conductivity of the diopside-tremolite-albite (Di-Tr-Ab) sample and the conductivity (insulation resistance) of the assembly (MgO) as a function of reciprocal temperature.

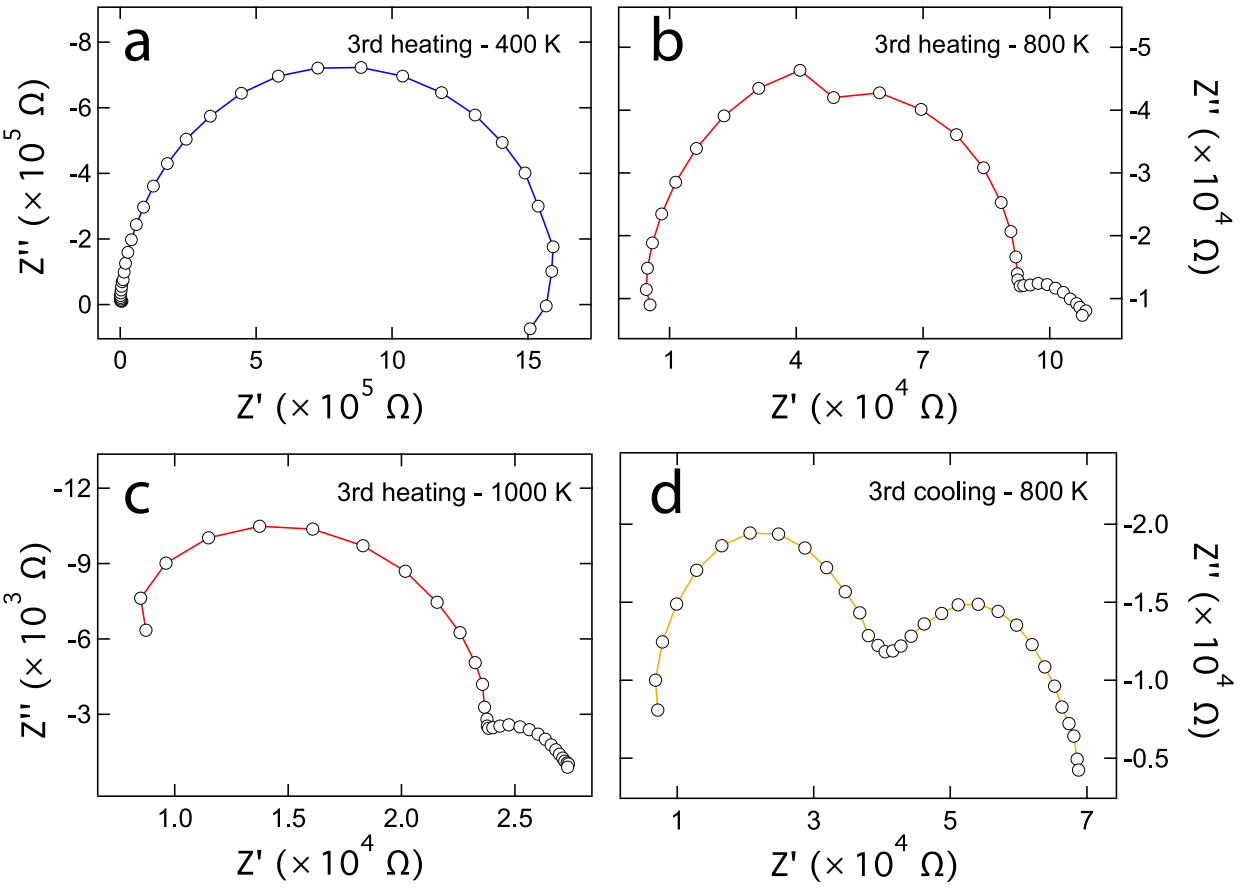

Figure S3. Cole-Cole plot for the diopside-tremolite-albite sample at 3.0 GPa. The axis represents the real (Z') and imaginary part (Z'') of the complex impedance. (**a**) The sample is in the solid state at 400 K of the 3rd heating path. (**b-c**) The radius of the arc continues to shrink and an additional arc is observed in the low-frequency range at 800 K and 1000 K of the 3rd heating path. (**d**) The separation of the two arcs is very clear at 800 K of the 3rd cooling path. The separation of the two arcs in panel (**b-d**) possibly indicates two conductive paths, one through the grain interior and the other one along the grain boundary. This probably reflects the dehydration of the amphibole-bearing rock sample which generates two conductive phases at high temperatures, i.e., the original solid phase and the aqueous fluid phase interconnected along the grain boundaries.

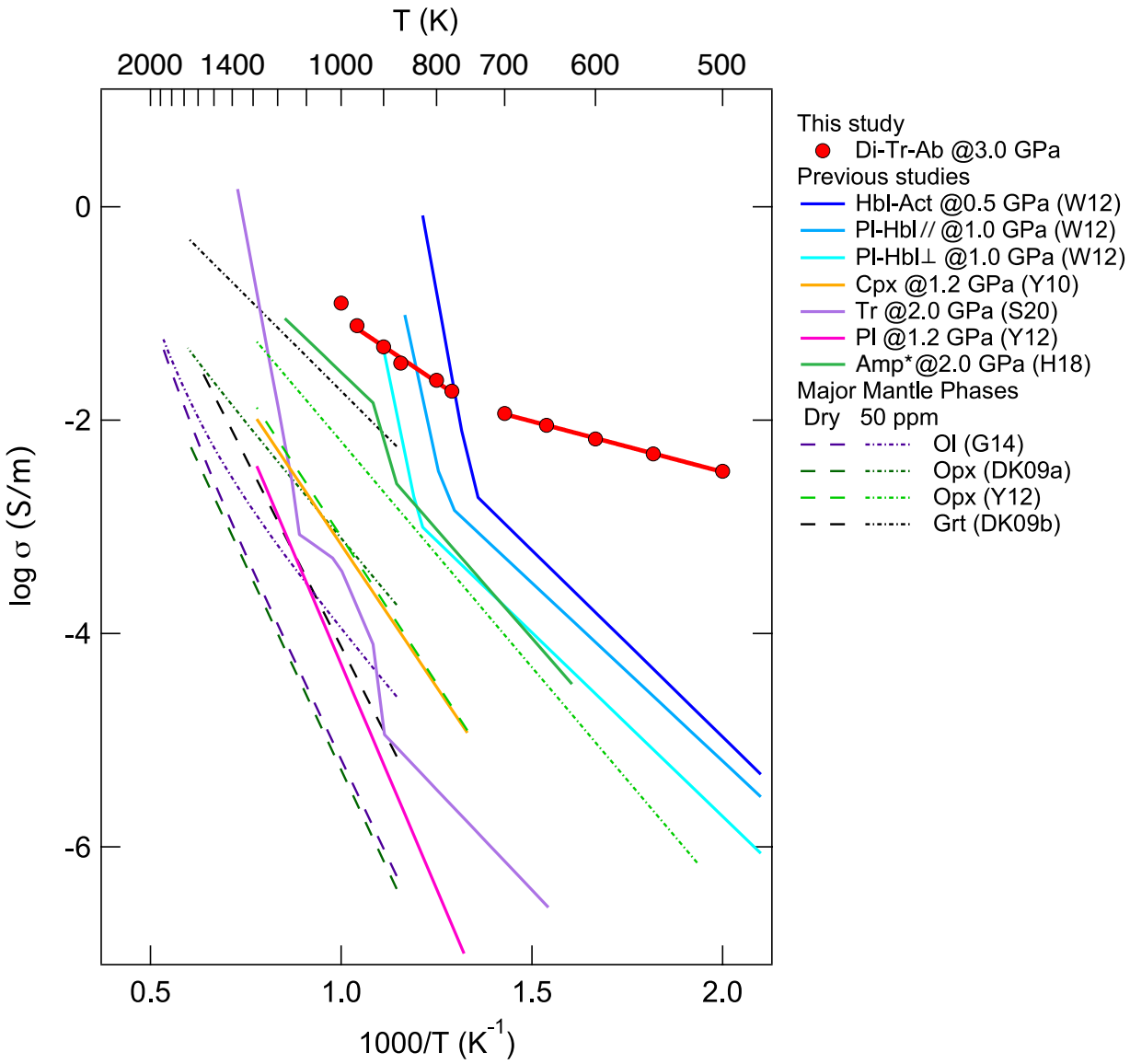

Figure S4. Plot of electrical conductivity of the diopside-tremolite-albite (Di-Tr-Ab) sample as a function of reciprocal temperature. Note: the filled red symbols- data from this study; the bold red lines- Arrhenius fit to data from this study; the dark blue line- hornblende-actinolite-bearing hornblendite (Hbl-Act) (W12: Wang et al., 2012); the intermediate blue line- plagioclase-hornblende-bearing hornblendite parallel to the lineation within the sample (Pl-Hbl//); the light blue line- plagioclase-hornblende-bearing hornblendite perpendicular to the lineation within the sample (Pl-Hbl⊥); the orange line- clinopyroxene (Cpx) (Y11: Yang et al., 2011); the purple line-

tremolite (Tr) (S20: Shen et al., 2020); the magenta line- plagioclase (Pl) (Y12: Yang et al., 2012); the green line- amphibole (Amp*) (H18: Hu et al., 2018); the thin dashed and dotted lines represent "dry" NAMs and "wet" NAMs with 50 ppm water, respectively: olivine (Ol) (G14: Gardés et al., 2014), orthopyroxene (Opx) (DK09a: Dai and Karato, 2009a; Y12: Yang et al., 2012), and garnet (Grt) (DK09b: Dai and Karato, 2009b).